WILEY | Hindawi

Research Article

Experimental Study on Grouting Seepage Characteristics of Single-Fractured Rock Masses with Different Inclination Angles under Three-Dimensional Stress

Hexuan Zhu [1] **and Lijun Han**[2]

[1]*College of Civil and Architecture Engineering, Chuzhou University, Chuzhou 239000, China*
[2]*State Key Laboratory for Geomechanics and Deep Underground Engineering, China University of Mining and Technology, Xuzhou, Jiangsu 221116, China*

Correspondence should be addressed to Hexuan Zhu; tb18220026b4@cumt.edu.cn

In underground engineering, the fracture dip angle and three-dimensional stress have great influence on the permeability and mechanical properties of fractured rock mass. Firstly, single-fracture samples with similar three-dimensional fractal dimensions and different dip angles were selected by using CT scanning technology. Then, the grouting material seepage tests under different dip angles and different three-dimensional stresses were carried out by self-developed single-fracture stress-seepage coupling true triaxial test system. The experimental data of stress-strain curve, grouting pressure, and grouting material flow rate of single-fracture specimen under different fracture dip angles and three-dimensional stress were obtained. The results show that the three-dimensional fractal dimension can be used as an index to measure the influence of fracture factors on grouting seepage test. The third principal stress σ_3 had a greater influence on the fracture width than the first principal stress σ_1. The larger the fracture inclination, the lower the strength of the single-fracture specimen. As the third principal stress σ_3 increases, the grouting pressure increased while the grouting flow decreased. With the increase of the fracture inclination angle, the influence of σ_1 on the hydraulic conductivity became larger, while the influence of σ_3 on the hydraulic conductivity became smaller. Moreover, the expression of hydraulic conductivity of single-fracture specimen with different dip angles under three-dimensional stress was obtained by nonlinear fitting of hydraulic conductivity data.

1. Introduction

Grouting technology has a history of more than 200 years and is widely used in tunnel, mine, foundation, pile foundation, and slope engineering. According to the engineering geological conditions of the roof coal and rock mass and the loose and broken characteristics of the coal mass that crosses the concentrated coal pillar, the coal and rock mass with the broken roof is usually reinforced by pregrouting. As a result, the stability and safety of the coal siding during the tunneling of the roadway and the open-off cut can be ensured, and an effective support structure can be formed in time [1–3]. The diffusion degree of grouting in fractured

coal and rock mass is mainly limited by the degree of fracture development of the surrounding rock itself and the distribution of the inclination of the fracture; on the other hand, it is mainly limited by the stress environment of the surrounding rock [4–6]. The stress state of the surrounding rock is the decisive factor for the opening degree of the fracture, and the degree of development of the surrounding rock fracture and the distribution of the inclination of the fracture determine the degree of influence of the fracture itself on the spread of the grout. The two influences on the spread of the grout are complementary and indispensable [7, 8]. Therefore, the study of grouting seepage in fractured rock masses with different fracture inclination angles under the action of
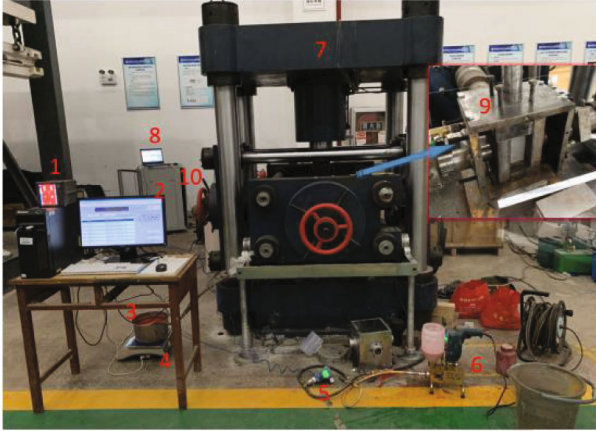
FIGURE 1: Three dimensional stress grouting system.

three-dimensional stress is of great significance for studying the law of grout diffusion in surrounding rocks and the plugging mechanism.

Fracture spacing, fracture flow, grouting pressure, slurry viscosity, roughness, and grouting material are the main physical parameters that affect the grouting seepage process [9–12]. The influence of fracture on slurry diffusion is mainly related to the characteristics of fracture itself. Fracture characteristics can be described by shape, size, and surface morphology, including fracture aperture, fracture opening angle, fracture development and extension direction (fracture curvature), and fracture surface roughness [13–18]. They all affect the fluid movement in fractures, such as flow rate, velocity, and flow pattern. Because the fracture is formed by tensile force, the surface of tensile fracture is rougher than that of shear fracture. Tensional fractures are widely distributed in nature, which is of great significance to the storage, water supply, and migration of groundwater. The roughness of fracture surface is an important factor affecting fracture fluid movement, but the quantitative description of rough surface morphology has been a long-term problem in fracture research [19–22].

In addition to the factors of the fracture itself, the in situ stress environment of the fracture also has an important influence on the fluid seepage. The surface and width of fracture are easily affected by external factors. Many studies focus on the flow behavior of fracture under normal stress [23–26]. Some researchers have studied the hydraulic characteristics of fractured rock mass based on shear stress from the perspectives of shear direction, contact area, shear displacement, and high water pressure [27–30]. Moreover, there are still many researchers trying to build the relationship between stress and fluid flow under confining pressure. Under confining pressure, the influence of pore pressure and effective stress coefficient on the permeability of fractured rock mass is studied [31–33]. However, in practical engineering, the grouted fracture has a certain dip angle and is in the complex geostress environment of three-dimensional stress, but there are few research results on fracture seepage characteristics under three-dimensional stress [34, 35], Moreover, the expression of hydraulic conductivity under three-dimensional stress still has some limitations, which

needs to be further improved [36–38]. The three-dimensional stress is the occurrence condition of the fractured rock mass, and the fracture dip angle is the geometric state of the fracture itself. These two aspects have mutual influence on the slurry migration in the fracture and are a pair of coupling factors [39–44]. In a word, the slurry diffusion in the fractured rock body needs to consider the slurry diffusion mechanism in the fractured rock body with different dip angles under the three-dimensional stress environment, which is the research direction that meets the needs of the project.

In this work, firstly, the single-fracture samples were scanned by CT to select the samples with similar three-dimensional fractal dimension. Then, the slurry seepage test under different inclination angle fractures and different three-directional principal stresses was carried out through the self-developed true triaxial stress-seepage coupling test system. The stress-seepage coupling mechanism of single fracture with different three-dimensional stresses and different fracture dip angles was studied. Finally, the hydraulic conductivity expressions of the single-fracture specimens of the inclination angle of each fracture under the three-dimensional stress were obtained.

2. Three Dimensional Stress Grouting System

The established three-dimensional stress grouting system is used to conduct grouting test on fractured rock mass (Figure 1). The true triaxial testing machine is used to realize the three-dimensional loading of the fractured rock mass. The sealing of the fractured rock mass during the grouting test is realized by the self-developed grouting test device. The specific components of the three-dimensional stress grouting system can refer to the published literature [39, 40].

In combination with the loading mode of the above true triaxial testing machine, a three-dimensional stress single-fracture rock mass stress-seepage coupling seepage grouting test device has been independently developed. The specific equipment process is shown in Figure 2. The sample is placed in the concave groove of the lower pressure plate (Figure 2(a)), the left and right pressure plates are installed on both sides of the sample as shown in Figure 2(b), and then, the upper pressure plate is covered on the sample. The upper and lower pressure plates and the left and right pressure plates are placed around the sample by rotation, and the four pressure plates are in a "spinning windmill shape" (Figure 2(c)). After that, it is placed on the frame, the upper slurry inlet pipe is installed on the lower pressure plate, and the upper slurry outlet pipe is installed on the upper pressure plate (Figure 2(d)). Then, the front pressure plate is placed in front of the sample and the front cover plate and the pressure column are installed. It is worth noting that the pressure column should bear against the front pressure plate to prevent the front pressure plate from falling back to the front cover plate; then tighten the nuts on the front cover plate, the upper cover plate, and the frame; and install the rear pressure plate, the rear cover plate, and the pressure column according to the same method, as shown
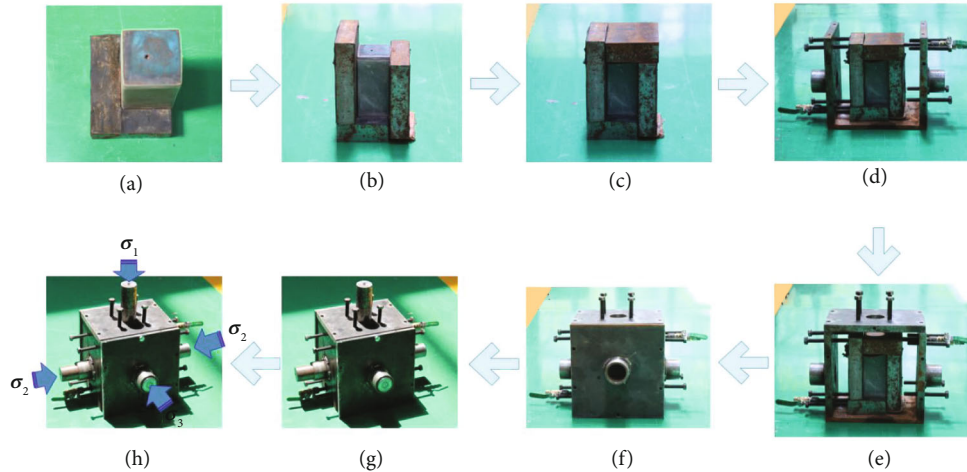
Figure 2: Equipment process of grouting test device.

in Figures 2(e)–2(g). Finally, the pressure columns in other principal stress directions are installed.

As shown in Figure 3, the grouting test device is equipped with various accessories. The size of the groove of the upper and lower pressing plates is 53 mm × 53 mm, so that the permeable plate and thick heat shrinkable pipe can be placed into the groove. The holes in the upper and lower pressure plates are directly opposite to the slurry inlet holes of the permeable plate to form a channel for slurry flow.

3. True Triaxial Test of Stress-Seepage Coupling of Single Fracture

3.1. Test Materials. Based on the basic mechanical properties of surrounding rock and the in situ stress environment in the project, samples with uniaxial compressive strength of 35~40 MPa are selected for the grouting test. The proportioning experiment was carried out according to the proportioning order of cement : quartz sand : water. The composition of quartz sand is quartz sand of two particle sizes added according to a fixed proportion $(30 - 50 \text{ mesh} : 70 - 120 \text{ mesh} = 2.5 : 1)$. The uniaxial compression test was carried out on the complete specimens of 9 proportions, and the stress-strain curves obtained are shown in Figure 4. After comparison, the ratio scheme of $1 : 0.7 : 0.55$ is selected as the standard ratio for the grouting test. The consolidated body with a volume of 0.125 m^3 was poured and cured for 30 days. In order to further determine the strength of the specimen, three standard specimens were drilled out of the consolidated body to conduct the uniaxial test again, as shown in Figure 4. The consolidated body was cut into small cubes and further polished to a size of 100 mm × 103 mm × 100 mm cube.

As shown in Figure 5, the sample is divided to obtain a single-fracture sample with middle penetration. Then, the sample was staggered about 1.5 mm along the left and right sides of the fracture. The 50 mm square red wire frame was drawn on one side of the sample, and the angles between one side of the wire frame and the fracture are set as 0°, 15°, and 30°, respectively. The rock plate was cut according to the red wire frame, and the single-fracture sample with 0°, 15°, and 30° inclination angle can be obtained, respectively. Therefore, these samples were processed into a cuboid of $50 \times 50 \times 100 \text{ mm}^3$. The above description is the production process of the sample to be subjected to the grouting test. The grouting material is ultrafine cement, and the water-cement ratio is 1.0.

Then, the fractures on both sides of the long side of the single-fracture specimen were sealed with hot melt adhesive. The single-slit specimen was scanned using medical CT (spatial resolution of $75 \mu\text{m}$) to obtain cross-sectional data of the single slit. Avizo three-dimensional reconstruction software was used for data processing to obtain the fractal dimension of single-fractured body. A single-fracture specimen with three-dimensional fractal dimension D_{3f} in a certain interval was selected for the test, and the three-dimensional fractal dimension interval of three-dimension single-fracture specimens is set to 2.121~2.171. The distribution of the corresponding two-dimensional fractal dimension D_{2f} with the height of the sample is shown in Figure 6. The upper and lower permeable plates are, respectively, placed at both ends of the sample and covered with rubber. Finally, the sample, permeable plate, and gasket are wrapped with a heat shrinkable tube with a thickness of 1 mm, and the area of the slurry inlet and the slurry outlet is reserved.

3.2. Test Scheme. In order to study the influence of three-dimensional stress on seepage grouting in single-fractured rock mass, the test scheme is formulated: when σ_2 is set as 10 MPa, σ_3 is set as 4 MPa, 6 MPa, 8 MPa, 10 MPa, and 12 MPa, respectively. The pressure of σ_1 is increased according to a certain gradient, and the sample is grouted every time the stress environment reaches a certain gradient. After the grouting pressure is stable, the grouting is stopped, and then, the next gradient stress is applied to σ_1 until σ_1 reaches 28 MPa. The specific grouting three-dimensional stress value is shown in Table 1.

(a)

(b)

(c)

(d)

(e)

(f)

Figure 3: Continued.

(g)

FIGURE 3: Equipment accessories of true triaxial penetration grouting test device. (a) Upper pressing plate; (b) σ_3-direction cover plate; (c) left and right pressing plates; (d) front and rear pressing plates; (e) frame; (f) upper cover plate; (g) slurry inlet pipe and slurry outlet pipe.
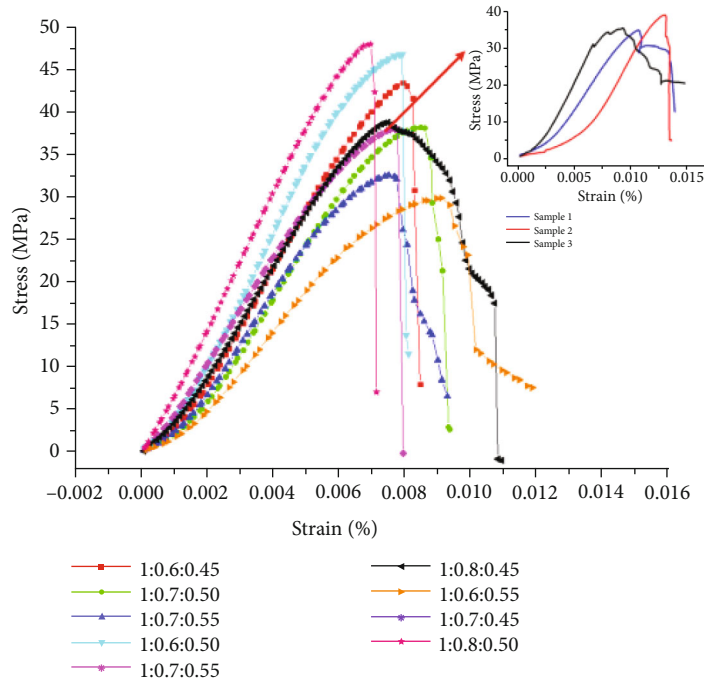

FIGURE 4: Stress-strain curve of the proportioned sample.

The loading mode of the test scheme is force loading, and the loading rate is 0.1 kN/s. When the three-dimensional prestressing force reaches 10 kPa, the three-dimensional stress is loaded together until it reaches the design value of stress in all directions. Taking the fracture dip angle of 15° and the stress setting state ($\sigma_2 - \sigma_3 = 8 - 6$ MPa) as an example, the loading path of the sample and the starting point of grouting time are shown in Figure 7. The difference is that the initial second principal stress σ_2 and the third principal stress σ_3 are different.

The samples were grouted at the same grouting rate. At the initial stage of grouting, the grouting pressure rises continuously. When the grouting pressure is stable to a certain

value, the grouting is continued for about 30 s, and then, the grouting is stopped. The grouting material is superfine cement with a water cement ratio of 1.0.

3.3. Analysis of Test Results

3.3.1. Stress-Strain Analysis. When the second principal stress σ_2 is 8 MPa, the variation of deviatoric stress-strain curve with an inclination angle of 15° under different third principal stresses σ_3 is shown in Figure 8. First of all, the single-fracture specimen is loaded from the three-dimensional prestress of 10 kPa to $\sigma_1/\sigma_2/\sigma_3 = 8/4/4$ MPa, which is the three-dimensional stress state indicated by the
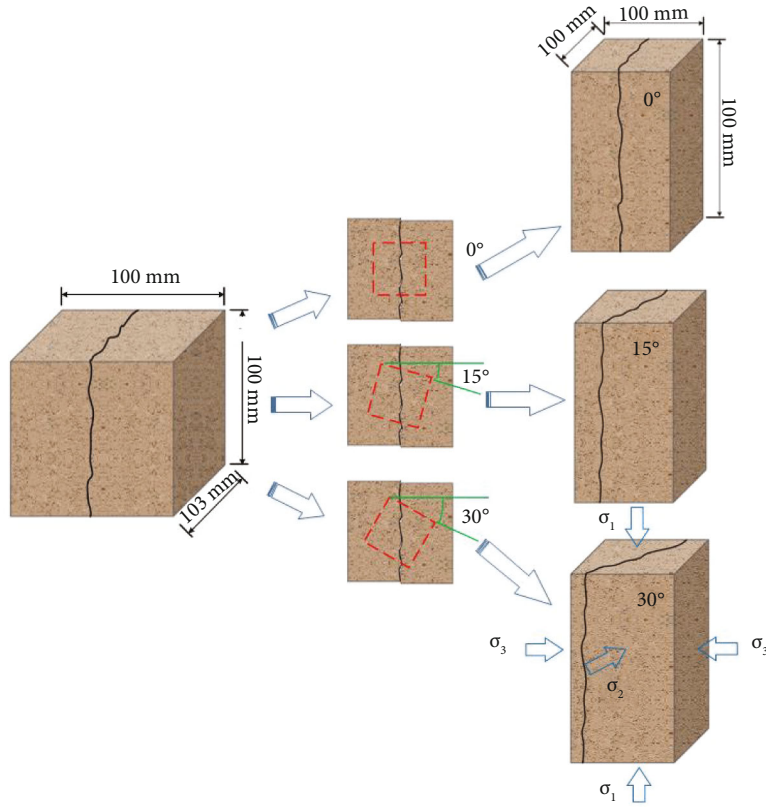
FIGURE 5: The manufacturing process of single-fracture specimens with different inclination angles.

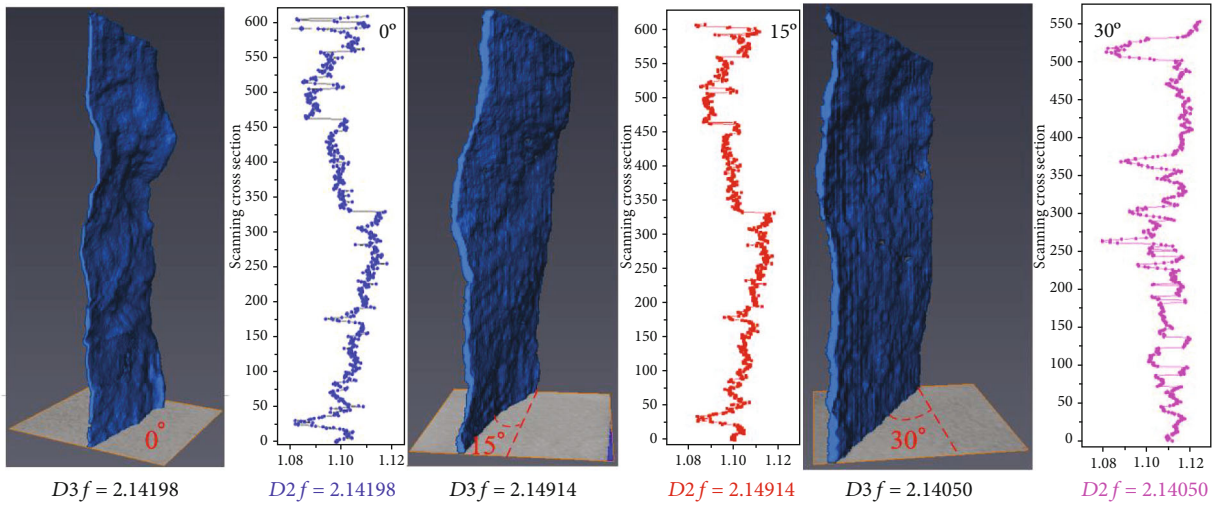| $D3f = 2.14198$ | $D2f = 2.14198$ | $D3f = 2.14914$ | $D2f = 2.14914$ | $D3f = 2.14050$ | $D2f = 2.14050$ |

FIGURE 6: Three-dimensional reconstruction of a single fracture and its fractal dimension.

TABLE 1: Three dimensional stress values of the grouting test.

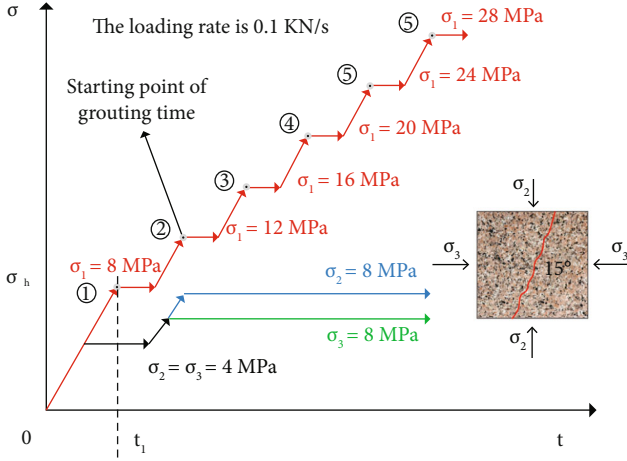| σ_2 (MPa)	σ_3 (MPa)	Grouting is carried out every time a certain stress environment ($\sigma_1 - \sigma_2 - \sigma_3$ (MPa)) is reached					
	4	8-4-4	12-10-4	16-10-4	20-10-4	24-10-4	28-10-4
	6	8-4-4	12-10-6	16-10-6	20-10-6	24-10-6	28-10-6
10	8	8-4-4	12-10-8	16-10-8	20-10-8	24-10-8	28-10-8
	10	8-4-4	12-10-10	16-10-10	20-10-10	24-10-10	28-10-10
	12	8-4-4	12-10-12	16-10-12	20-10-12	24-10-12	28-10-12

FIGURE 7: Loading path and grouting time.

black dotted line in the figure. As shown in Figure 7, the three-dimensional stress state marked by the black dotted line is the time point of the first grouting. This process is the same for each test scheme, and the ε_3 of the sample under this stress environment all reached about 0.4%.

After the specimen is continuously loaded, each test loading path in Figure 8 reached the stress state, respectively: σ_1 is 12 MPa, σ_2 is 10 MPa, and σ_3 is 4 MPa, 6 MPa, 8 MPa, 10 MPa, and 12 MPa, respectively. At this time, the second grouting time point has been reached, and the strain has changed a lot during this loading process, and the strains ε_3 reached 0.401%, 0.712%, 0.780%, 0.902%, and 1.899%, respectively, as shown in Figures 8 and 9. With the increase of σ_3, the deflection of stress-strain curve between the time point of the first grouting and the time point of the second grouting is more and more bending. This is because the three-dimensional stresses all are loaded at 0.1 kN/s, but the loading rate for σ_1 is equivalent to 0.04 MPa/s, and σ_3 is equivalent to 0.02 MPa/s. The loading rate of σ_1 is greater than σ_3, which caused the deviatoric stress $(\sigma_1 - \sigma_3)$ to increase first and then decrease. After that, σ_2 and σ_3 remain unchanged, and σ_1 is loaded according to a certain stress gradient until it reaches 28 MPa. In this loading process, the influence on ε_2 and ε_3 is small, while ε_1 is increasing, as shown in Figures 8–10.

As shown in Figure 9, different σ_3 has a great influence on ε_3. When σ_3 reached 12 MPa, ε_3 is close to 2%. It can be inferred that the single-fracture specimen with an inclination angle of 15° is likely to be destroyed in the third principal stress direction when it reached the stress state of $\sigma_1/\sigma_2/\sigma_3 = 12/8/12$ MPa. As shown in Figure 10, with the increase of σ_3, ε_1 decreases gradually; ε_1 are 1.319%, 1.058%, 0.981%, 0.968%, andc0.905%, respectively; and the reduction rates are 19.787%, 7.278%, 1.325%, and 6.508%, respectively. With the increase of σ_3, the influence of σ_3 on ε_1 decreases gradually, regardless of the case that σ_3 is 12 MPa. When σ_3 is 12 MPa, the difference between ε_3 and other experimental schemes is mainly because σ_1 is only loaded to 24 MPa but not to 28 MPa.

As shown in Table 2, with the increase of σ_3, ε_1 and ε_2 of samples with different inclination angles generally show a decreasing trend, except that the inclination angle is 30°. When the dip angle of fracture is 30°, ε_1 and ε_2 first decrease and then increase with the increase of σ_3. When the dip angle of fracture is 15° and σ_3 is 12 MPa, the phenomenon of growth also appeared in ε_2. This shows that the larger the fracture angle is, the easier the specimen will be damaged when σ_3 increases to a certain value. The above conclusion can also be verified from the increasing degree of ε_3. The larger the fracture angle, the greater the increasing degree of ε_3, indicating that the specimen is more prone to fracture. According to the data in Table 2, the variation curves of volumetric strain ε_V under different fracture dip angles and σ_3 are obtained.

As shown in Figure 11, on the whole, the larger the fracture angle increases, the larger the volumetric strain. This indicates that the larger the fracture inclination angle, the weaker the deformation resistance of the sample. When the fracture angle is 15° and σ_3 is 12 MPa, the increment of volumetric strain increases greatly, while when the fracture angle is 30° and σ_3 is 10 MPa, the increment of volumetric strain increases greatly. The phenomenon that the increment of the above volumetric strain increases greatly indicates that a new crack has occurred in the sample and also reflects that the larger the fracture angle is, the lower the strength of the sample is, as shown in Figure 12.

3.3.2. Analysis of Grouting Pressure. Figure 13 shows the variation curve of grouting pressure with grouting time for a single-fracture specimen with an inclination angle of 15° under different three-dimensional stresses. The grouting pressure rises rapidly at first, and finally, it can be stabilized at a certain pressure value, which indicates that the grouting achieves stable seepage. On the whole, the grouting pressure increases with the increase of σ_3. When the three-dimensional stress is $\sigma_1/\sigma_2/\sigma_3 = 8/4/4$ MPa, the grouting pressures in Figures 13(a)–13(e) are 70 kPa, 69 kPa, 85 kPa, 78 kPa, and 80 kPa, respectively, which are basically maintained at a pressure level, indicating that the three-dimensional fractal dimension index of the single-fracture sample with 15° can measure the influence of fracture factors on the grouting pressure.

When loading to the stress state of the second grouting time point, with the increase of σ_3, the stable value of grouting pressure increases sharply. According to the analysis of Figures 8 and 9, during the loading of stress state from the first grouting time point to the second grouting time point, ε_3 increases greatly. Therefore, it can be inferred that this is mainly caused by the increase of σ_3 which leads to the significant decrease of fracture width. After that, the grouting pressure increases uniformly with the increase of σ_1. This phenomenon can also be verified from the analysis in Figures 8 and 9. The increase of σ_1 has little effect on ε_3, but ε_1 increases gradually. The above analysis shows that the movement of the rock plate on both sides of the fracture is small, but the axial compression results in the reduction of the total volume of the sample, which leads to the axial shrinkage of the rock plate and the expansion of the third
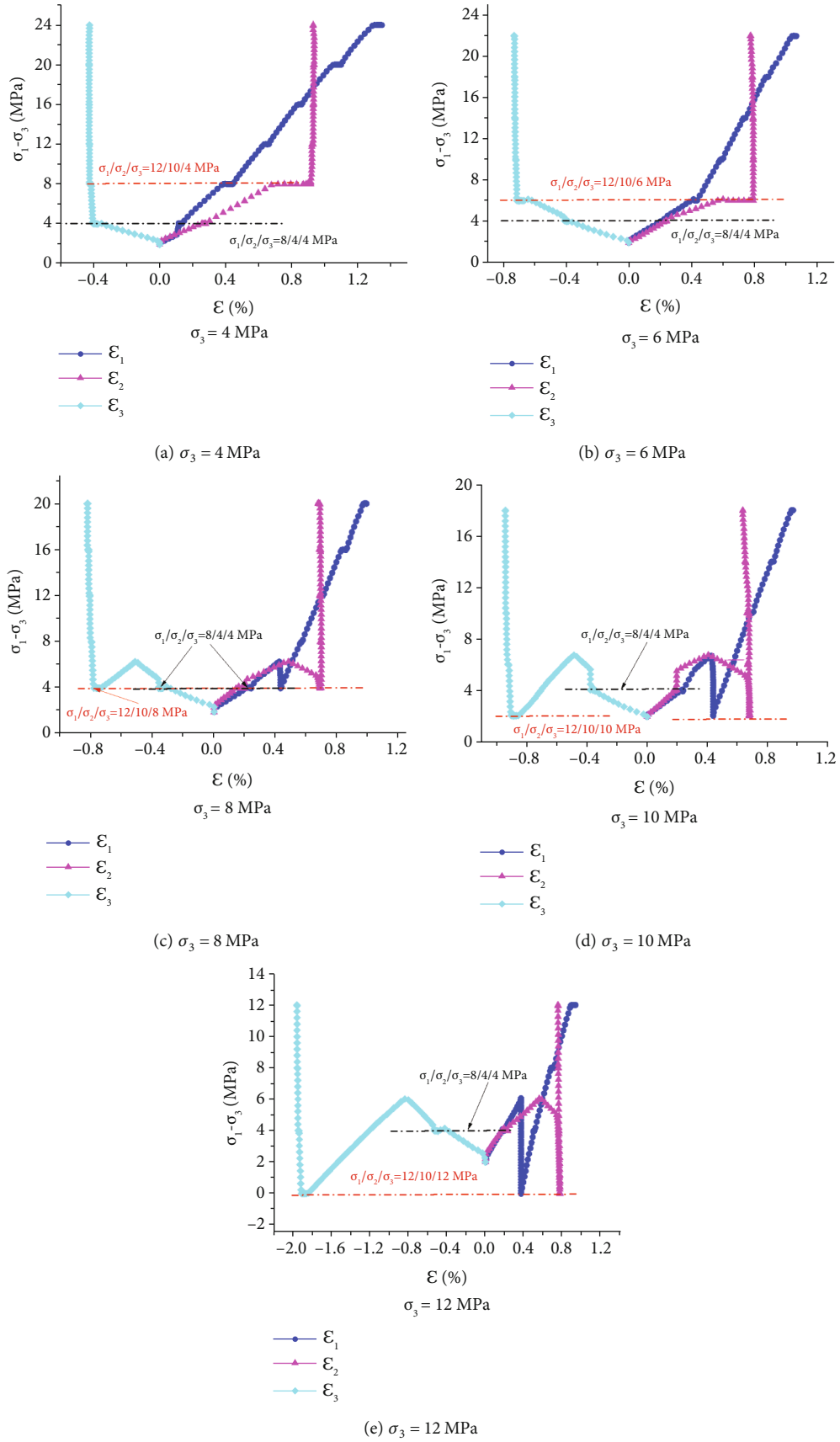
(a) $\sigma_3 = 4$ MPa

(b) $\sigma_3 = 6$ MPa

(c) $\sigma_3 = 8$ MPa

(d) $\sigma_3 = 10$ MPa

(e) $\sigma_3 = 12$ MPa

Figure 8: Deviatoric stress-strain of grouting sample under three-dimensional stress.
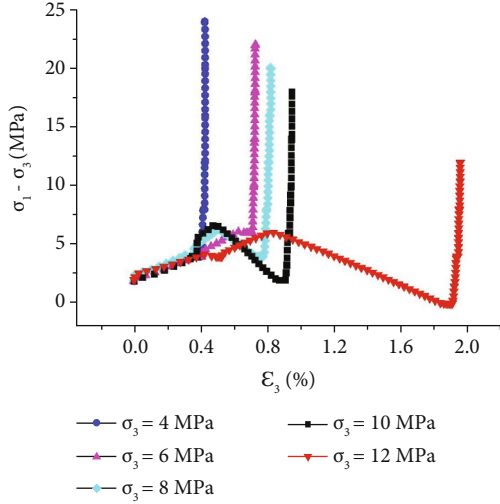
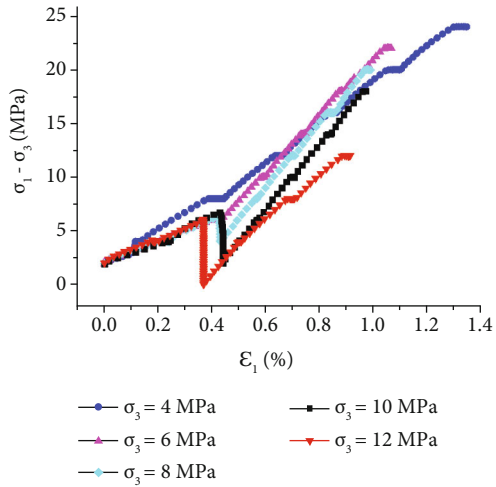FIGURE 9: Deviatoric stress-strain (ε_3) relationship under different σ_3.

FIGURE 10: Deviatoric stress-strain (ε_1) relationship under different σ_3.

TABLE 2: Strain of each principal stress direction under different triaxial stresses and fracture dip angles.

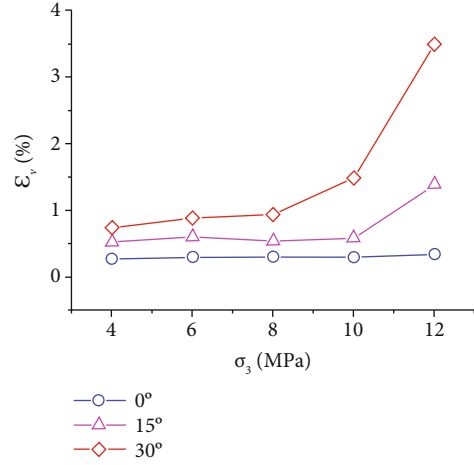| Dip angle (θ) (°)	ε (%)	$\sigma_3 = 4$ MPa	$\sigma_3 = 6$ MPa	$\sigma_3 = 8$ MPa	$\sigma_3 = 10$ MPa	$\sigma_3 = 12$ MPa
0	ε_1	1.08	0.8728	0.7896	0.7592	0.7404
	ε_2	0.7464	0.6224	0.5484	0.5104	0.5032
	ε_3	0.3408	0.564	0.696	0.7976	0.9296
15	ε_1	1.35	1.066	0.987	0.974	0.938
	ε_2	0.933	0.778	0.673	0.638	0.754
	ε_3	0.426	0.73	0.82	0.947	1.962
30	ε_1	1.46475	1.22625	1.119375	1.21275	1.41525
	ε_2	1.058625	0.88425	0.757125	0.87075	1.11825
	ε_3	0.47925	0.82125	1.1025	1.407375	2.20725

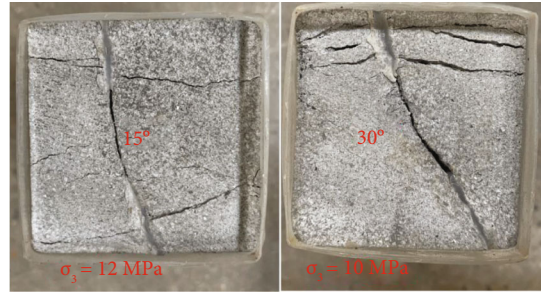FIGURE 11: Volume strain ε_V of single-fracture specimen.

FIGURE 12: Physical picture of fracture of single-fracture specimen.

principal stress direction. The expansion volume in the third principal stress direction is mainly used to compress the space between fractures or to fill the gap between fractures, and a small part of the expansion volume results in a small increase of ε_3. In Figure 13(e), when the three-dimensional stress state is $\sigma_1/\sigma_2/\sigma_3 = 24/8/10$ MPa, the grouting pressure increases continuously. In order to avoid the burst of grouting pipeline, the grouting is stopped when the grouting pressure rises to about 6 MPa, which is defined as nongrouting stress state in the test. This phenomenon is also corresponding to the phenomenon that ε_3 is close to 2% in Figures 8 and 9. When σ_3 is applied to 12 MPa (greater than σ_2), ε_3 increases greatly, and then, the loading of σ_1 is prone to be noninjectable.

3.3.3. Slurry Flow Analysis. Figure 14 shows the variation curve of cumulative flow rate of slurry with grouting time for single-fracture samples with 15° dip angle under different three-dimensional stresses. The cumulative flow of slurry in each stress state in the figure shows a linear growth, which indicates that the slurry flow is a certain value; that is, the slurry reaches a stable seepage. The reason for the difference of the final value of slurry cumulative flow is that the grouting time is different, which has no correlation with the flow value. According to the observation of the change of σ_1, the slurry flow decreases with the increase of σ_1 under the action of different σ_3. The same conclusion can be drawn from Figure 15.
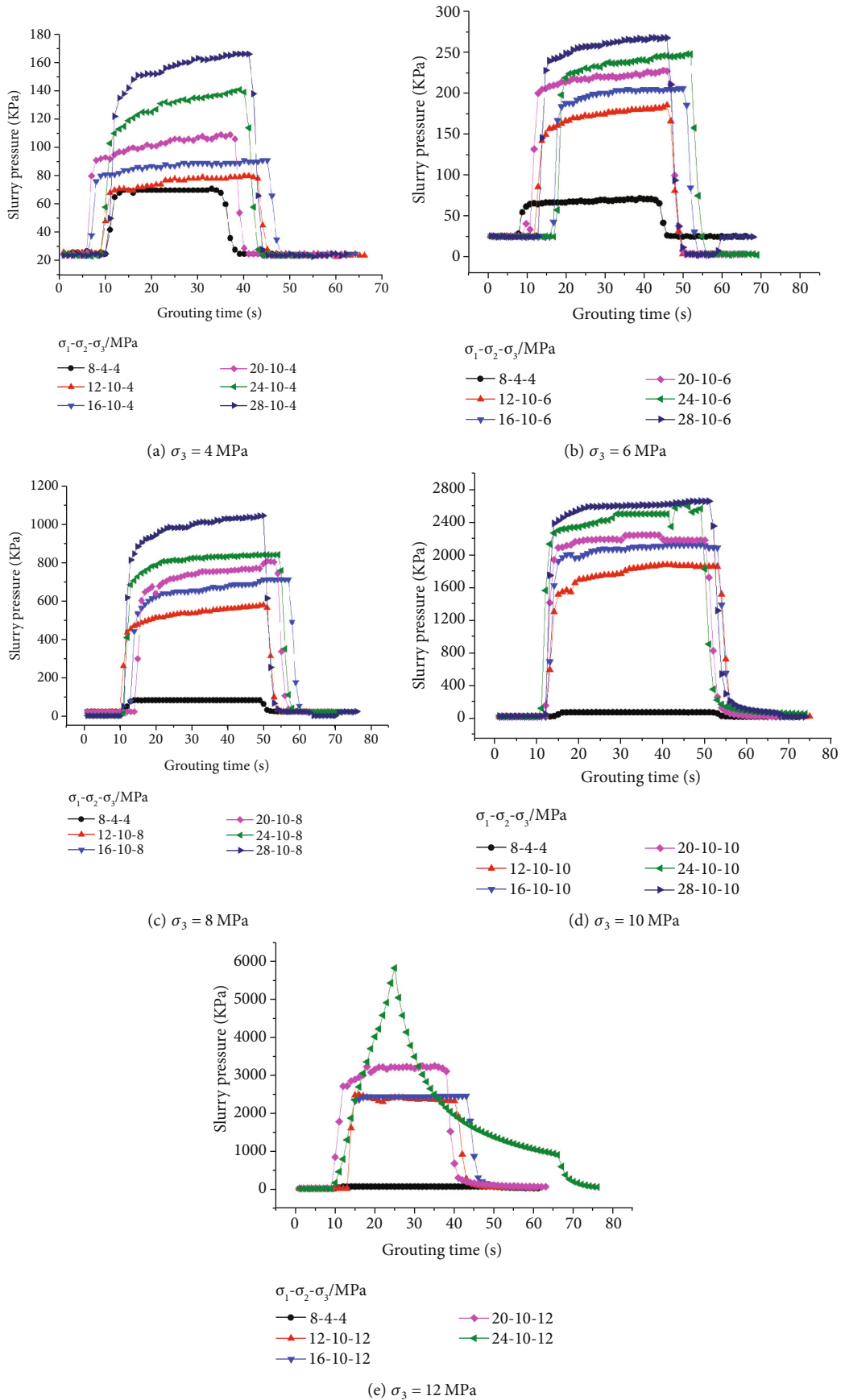
(a) $\sigma_3 = 4$ MPa

(b) $\sigma_3 = 6$ MPa

(c) $\sigma_3 = 8$ MPa

(d) $\sigma_3 = 10$ MPa

(e) $\sigma_3 = 12$ MPa

FIGURE 13: Grouting pressure under different three-dimensional stress states.

(a) $\sigma_3 = 4$ MPa

(b) $\sigma_3 = 6$ MPa

(c) $\sigma_3 = 8$ MPa

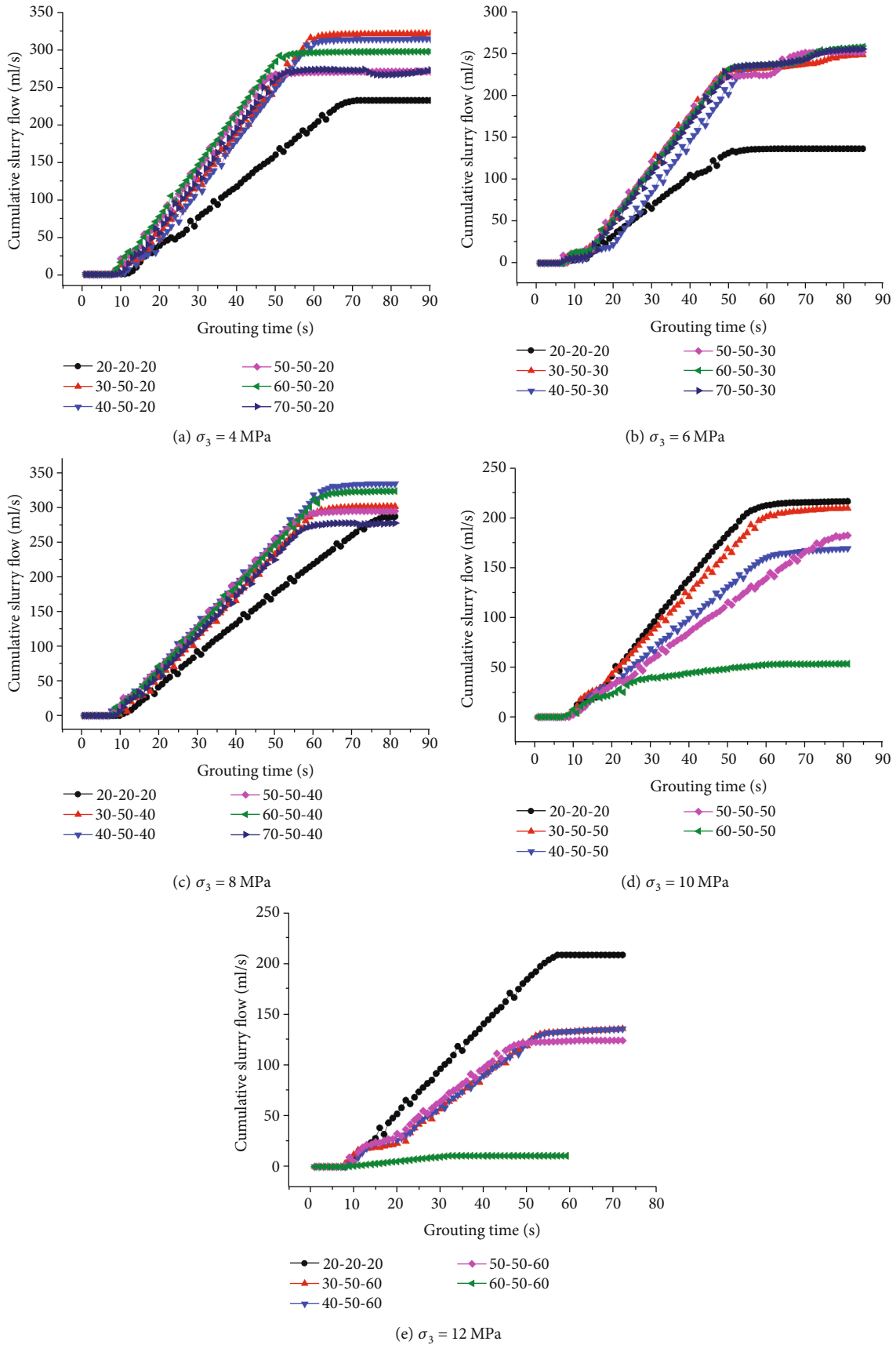(d) $\sigma_3 = 10$ MPa

(e) $\sigma_3 = 12$ MPa

FIGURE 14: Cumulative flow under different three-dimensional stress states.
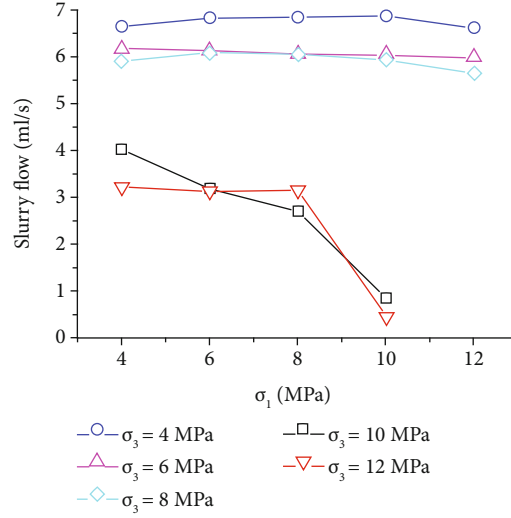
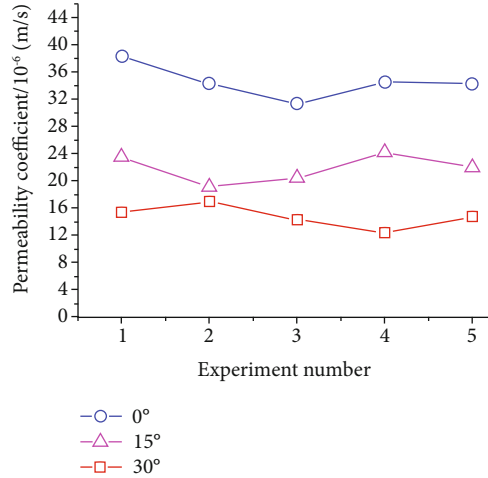FIGURE 15: Flow rate under three-dimensional stress.

FIGURE 16: Hydraulic conductivity of initial three-dimensional stress state.

The change rate of slurry cumulative flow is slurry flow; in other words, the slope of slurry cumulative flow curve is slurry flow. When σ_3 is 4-8 MPa, the change trend of slurry flow is basically the same. With the increase of σ_3 to 10 MPa, the slurry flow rate suddenly decreases, and the decrease amplitude is similar, as shown in Figure 15. This shows that the influence of σ_3 on slurry flow is greater than that of σ_1, in the stress range set in this test.

3.3.4. Hydraulic Conductivity Analysis. The water cement ratio used in this test is large, and the fluidity of the slurry is large. The slurry seepage can be regarded as Darcy seepage, and the slurry seepage coefficient can be obtained according to the following formula:

$$k_f = \frac{\rho g h}{d^2} \cdot \frac{Q}{\Delta P}, \tag{1}$$

where ρ is the density of slurry, $\rho = 1480\,\mathrm{kg/m_3}$; G is the

gravity coefficient, $G = 10\,\mathrm{N/kg}$; h is the height of sample, $h = 0.1\,\mathrm{m}$; D is the width or length of sample, $D = 0.05\,\mathrm{m}$; q is the grouting pressure; and ΔP is the difference between grouting pressure and slurry discharge pressure. In the test, the slurry outlet pipe is connected to the atmosphere, and the height of the sample is small, so ΔP can be approximately regarded as the grouting pressure P, $\Delta P = P$. According to the data in Figures 13 and 15, the seepage coefficient is obtained, as shown in Figures 16 and 17. Figure 16 shows the hydraulic conductivity of single-fracture specimens with different dip angles under the initial three-dimensional stress ($\sigma_1/\sigma_2/\sigma_3 = 8/4/4\,\mathrm{MPa}$). It can be seen that the hydraulic conductivity of samples with single fracture at each dip angle is basically maintained at a level, indicating that the optimized three-dimensional fractal dimension index of samples with single fracture at each dip angle can measure the influence of fracture factors on grouting pressure, which is corresponding to the relevant conclusions in grouting pressure analysis.
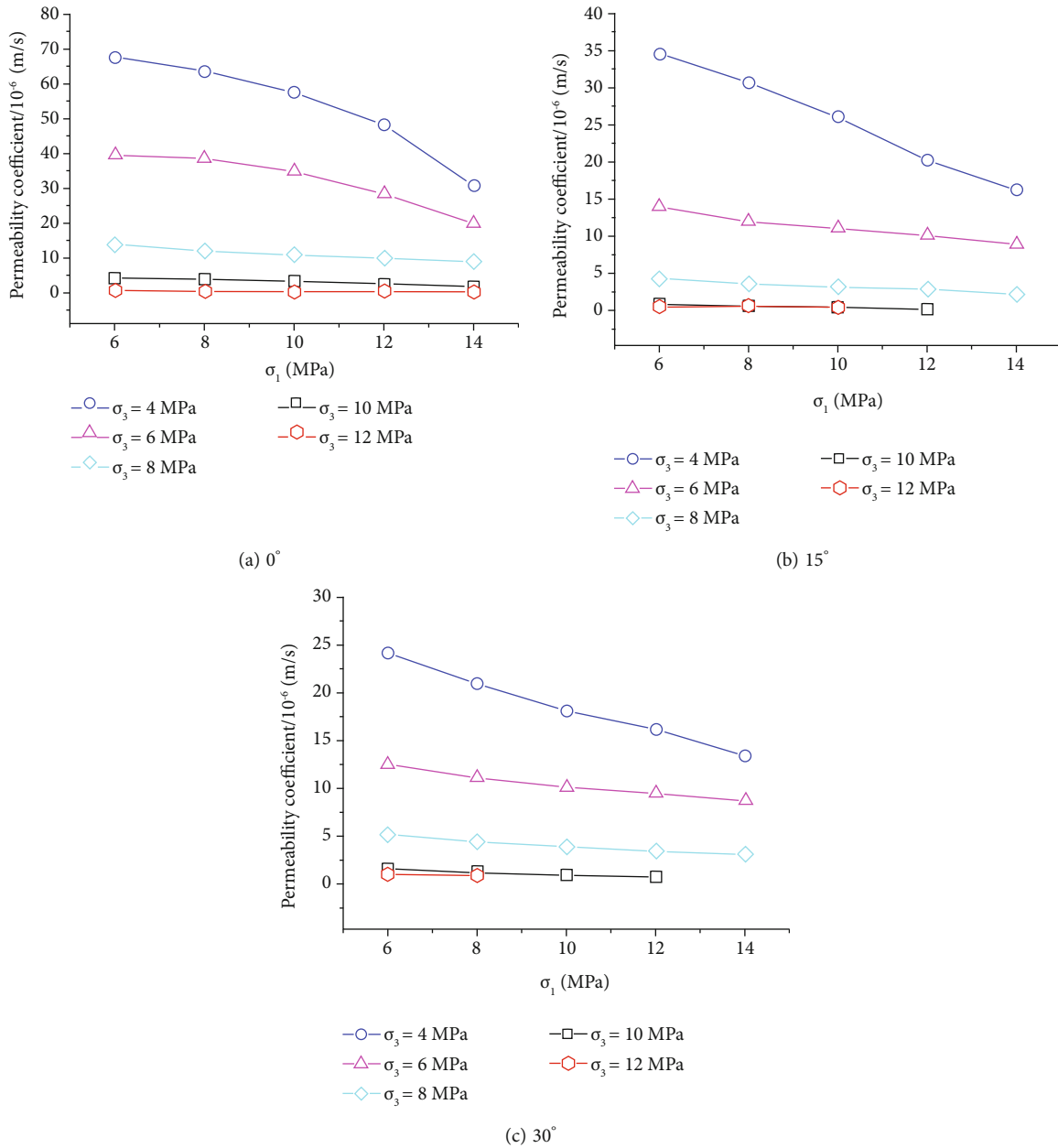
(a) 0°

(b) 15°

(c) 30°

FIGURE 17: Hydraulic conductivity under three-dimensional stress.

Figure 17 shows the hydraulic conductivity of single-fracture specimens with different dip angles under different three-dimensional stresses. The hydraulic conductivity of the single-fracture specimens with dip angles of 0°, 15°, and 30° gradually developed from convex to linear with the increase of σ_1, indicating that the degree of the influence of σ_1 on the hydraulic conductivity is increasing as the inclination angle increases. The hydraulic conductivity decreases with the increase of σ_3 for single-fracture samples with dip angles of 0°, 15°, and 30°, and the degree of decrease decreases with the increase of dip angle, which indicates that the degree of influence of σ_3 on hydraulic conductivity decreases with the increase of dip angle.

The prominent phenomenon is that when the single fracture with a dip angle of 15° and 30° appears noninjectable phenomenon, the three-dimensional stress state is, respectively, $\sigma_1/\sigma_2/\sigma_3 = 24/8/12$ MPa and $\sigma_1/\sigma_2/\sigma_3 = 24/8/10$ MPa. It can be concluded that the larger the dip angle and the larger the σ_1 and σ_3, the worse the injectability of the sample. Many research results have studied the influence of different three-dimensional stresses on hydraulic conductivity under true triaxial and summarized the calculation formula of hydraulic conductivity through fitting. It can be seen from the expression of the hydraulic conductivity of the above research results that the coefficients of σ_1 and σ_2 are regarded as the same value without considering the pore

water pressure, and the coefficient of σ_3 is regarded as another value. Then, the expression of hydraulic conductivity can be expressed as

$$k_f = k_{fi} \exp\left[a(-\sigma_1) + b(-\sigma_2) + c(-\sigma_3)\right]. \qquad (2)$$

Among them, a, b, and c are undetermined parameters, and K_{fi} is the hydraulic conductivity under the initial three-dimensional stress environment. The initial three-dimensional stress of this test is set as $\sigma_1/\sigma_2/\sigma_3 = 8/4/4$ MPa. Many variables in the theoretical formula are difficult to be measured directly through experiments, and it is time-consuming and laborious. 1stOpt software is based on excellent global optimization algorithm, which overcomes the problem that the initial value must be given in iterative calculation. Users can get the optimal solution without assigning parameters. 1stOpt software is the world's leading nonlinear fitting tool [35–37]. The coefficient c in Equation (2) is regarded as a variable constant, and the change values are set as 4, 6, 8, 10, and 12. The data in Figure 17 are fitted by universal global optimization algorithms, and the hydraulic conductivity expression of single-fracture sample with each dip angle under three-dimensional stress is obtained as follows:

$$\begin{cases} k_{f0} = 3.45535 \times 10^{-7} \times \exp\left[0.07633 \times (-\sigma_1) + 1.64686 \times 10 + 0.3609 \times (-\sigma_3)\right], \theta = 0° \left(R^2 = 0.985\right), \\ k_{f15} = 2.18734 \times 10^{-7} \times \exp\left[0.08495 \times (-\sigma_1) + 1.6705 \times 10 + 0.47508 \times (-\sigma_3)\right], \theta = 15° \left(R^2 = 0.982\right), \\ k_{f30} = 1.47995 \times 10^{-7} \times \exp\left[0.06549 \times (-\sigma_1) + 1.61877 \times 10 + 0.37169 \times (-\sigma_3)\right], \theta = 30° \left(R^2 = 0.978\right). \end{cases} \qquad (3)$$

The vertical principal stress can generally be estimated based on the thickness of the overlying rock layer. According to the Chinese geological research data, the rock bulk density is generally taken as 0.026 MPa/m. Therefore, the relationship between the vertical principal stress and the depth is approximately as follows:

$$\sigma_V = 0.026H,$$

Maximum horizontal principal stress : $\sigma_H = 0.0206H + 4.980,$

Minimum horizontal principal stress : $\sigma_H = 0.0096H + 3.286.$

$$(4)$$

Therefore, according to the in situ stress distribution law of Jincheng mining area in Shanxi Province, China, the in situ stress of Wujia coal mine (roadway 380-427 m, taken as 400 m) can be predicted as follows: $\sigma_V = 10.40$ MPa, $\sigma_H = 13.22$ MPa, and $\sigma_h = 7.126$ MPa. The maximum horizontal in situ stress is generally in the north-east direction, the in situ stress field type is $\sigma_H > \sigma_V > \sigma_h$, and the in situ stress is mainly horizontal stress. Therefore, substituting the above-mentioned stress value into Equation (3) can obtain the hydraulic conductivity of each fracture inclination. When the in situ stress monitoring is performed on the coal rock mass in the pregrouted area or the grouted roadway, a more accurate hydraulic conductivity distribution of the fractured rock mass can be obtained according to Equation (3). Furthermore, the monitored in situ stress data is used as the stress applied value in the laboratory test. According to this test method, the minimum injectable pressure distribution of the grout can be obtained and the grout volume can be calculated. The research team will conduct further research and application in the later scientific research work and provide basic data support as a grouting scheme design.

4. Conclusion

The influence of the third principal stress σ_3 on the fracture width is greater than that of the first principal stress σ_1 under the setting of stress level and loading path in this test. Within the set level of fracture angle in this experiment, the larger the fracture angle is, the lower the strength of single-fracture specimen is. Under the same σ_3 and if the value of σ_3 is large enough, the larger the fracture angle is, the easier the specimen is to fracture.

The grouting pressure has a stable period, and the slope of grouting cumulative flow is unique, which indicates that the grouting seepage test has reached the degree of stable seepage. Generally, with the increase of the third principal stress σ_3, the grouting pressure increased and the grouting flow decreased. In addition, in the initial stress environment, the grouting pressure, grouting flow, and hydraulic conductivity can verify that the three-dimensional fractal dimension is enough to measure the influence of fracture factors on the grouting seepage test.

With the increase of the first principal stress σ_1 or the third principal stress σ_3, the hydraulic conductivity decreased. The increase of the inclination angle of the fracture caused the degree of the influence of σ_1 on the hydraulic conductivity to increase, while the degree of the influence of σ_3 on the hydraulic conductivity showed a decreasing trend. Moreover, the hydraulic conductivity expressions of the single-fracture specimens at various dip angles under the three-dimensional stress were obtained by nonlinear fitting to the hydraulic conductivity data.

Data Availability

The data used to support the findings of this study are available from the corresponding author upon request.

Conflicts of Interest

The authors declare that they have no conflict of interest.

Acknowledgments

References

[1] B. Li, Y. Jiang, T. Koyama, L. Ling, and Y. Tanabashi, "Experimental study of the hydro-mechanical behavior of rock joints using a parallel-plate model containing contact areas and artificial fractures," *International Journal of Rock Mechanics and Mining Sciences*, vol. 45, no. 3, pp. 362–375, 2008.

[2] H. Stille, *Rock Grouting-Theories and Applications*, BeFo, Stockholm, 2015.

[3] H. Strømsvik and B. Gammelster, "Investigation and assessment of pre-grouted rock mass," *Bulletin of Engineering Geology and the Environment*, vol. 79, no. 5, pp. 2543–2560, 2020.

[4] C. Butron, M. Axelsson, and G. Gustafson, "Silica sol for rock grouting: laboratory testing of strength, fracture behaviour and hydraulic conductivity," *Tunnelling and Underground Space Technology*, vol. 24, no. 6, pp. 603–607, 2009.

[5] R. Gothäll and H. Stille, "Fracture-fracture interaction during grouting," *Tunnelling and Underground Space Technology Incorporating Trenchless Technology Research*, vol. 25, no. 3, pp. 199–204, 2010.

[6] W. Ding, C. Duan, and Q. Zhang, "Experimental and numerical study on a grouting diffusion model of a single rough fracture in rock mass," *Applied Sciences*, vol. 10, no. 20, p. 7041, 2020.

[7] R. Karagüzel and R. Kiliç, "The effect of the alteration degree of ophiolitic melange on permeability and grouting," *Engineering Geology*, vol. 57, no. 1-2, pp. 1–12, 2000.

[8] D. S. Park and J. Oh, "Permeation grouting for remediation of dam cores," *Engineering Geology*, vol. 233, pp. 63–75, 2018.

[9] L. P. Chegbeleh, M. Nishigaki, J. A. Akudago, and T. Katayama, "Experimental study on ethanol/bentonite slurry injection into synthetic rock fractures: application to seepage control," *Applied Clay Science*, vol. 45, no. 4, pp. 232–238, 2009.

[10] J. R. Chai and W. J. Cui, "Optimum thickness of curtain grouting on dam foundation with minimum seepage pressure resultant," *Structural and Multidisciplinary Optimization*, vol. 45, no. 2, pp. 303–308, 2012.

[11] G. Y. Lu, Y. S. Wang, Y. Q. Zhang, and S. T. Ariaratnam, "Feasibility of using sodium silicate as grouting in loose coal bed sections for methane drainage," *Tunneling and Underground Space Technology*, vol. 72, pp. 107–113, 2018.

[12] M. J. Li, M. R. Du, F. M. Wang, B. H. Xue, C. Zhang, and H. Y. Fang, "Study on the mechanical properties of polyurethane (PU) grouting material of different geometric sizes under uniaxial compression," *Construction and Building Materials*, vol. 259, p. 119797, 2020.

[13] S. R. Brown, "Fluid flow through rock joints: the effect of surface roughness," *Journal of Geophysical Research*, vol. 92, no. B2, pp. 1337–1347, 1987.

[14] R. W. Zimmerman and G. S. Bodvarsson, "Hydraulic conductivity of rock fractures," *Transport in Porous Media*, vol. 23, no. 1, pp. 1–30, 1996.

[15] N. Barton and E. F. de Quadros, "Joint aperture and roughness in the prediction of flow and groutability of rock masses," *International Journal of Rock Mechanics and Mining Sciences*, vol. 34, no. 3-4, pp. 252.e1–252.e14, 1997.

[16] Y. F. Chen, M. M. Liu, S. H. Hu, and C. B. Zhou, "Non-Darcy's law-based analytical models for data interpretation of high-pressure packer tests in fractured rocks," *Engineering Geology*, vol. 199, pp. 91–106, 2015.

[17] G. Rong, D. Hou, J. Yang, L. Cheng, and C. B. Zhou, "Experimental study of flow characteristics in non-mated rock fractures considering 3D definition of fracture surfaces," *Engineering Geology*, vol. 220, pp. 152–163, 2017.

[18] L. Gan, Z. Z. Shen, and M. Xiao, "Experimental investigation of seepage characteristics in porous rocks with a single fracture," *Hydrogeology Journal*, vol. 28, no. 8, pp. 2933–2946, 2020.

[19] N. Barton and V. Choubey, "The shear strength of rock joints in theory and practice," *Rock Mechanics*, vol. 10, no. 1-2, pp. 1–54, 1977.

[20] Y. H. Lee, J. R. Carr, D. J. Barr, and C. J. Haas, "The fractal dimension as a measure of the roughness of rock discontinuity profiles," *International Journal of Rock Mechanics and Minings Sciences*, vol. 27, no. 6, pp. 453–464, 1990.

[21] G. M. Lomize, *Flow in Fractured Rocks*, Gosemergoizdat, Moscow, 1951.

[22] H. Zhou and H. Xie, "Fractal description of rock joint opening," *Quarterly Journal of Engineering Geology & Hydrogeology*, vol. 1, pp. 1–4, 1999.

[23] Z. Zhao, L. Jing, I. Neretnieks, and L. Moreno, "Analytical solution of coupled stress-flow-transport processes in a single rock fracture," *Computers & Geoences*, vol. 37, no. 9, pp. 1437–1449, 2011.

[24] Z. Y. Zhang, J. Nemcik, and S. Q. Ma, "Micro- and macrobehaviour of fluid flow through rock fractures: an experimental study," *Hydrogeology Journal*, vol. 21, no. 8, pp. 1717–1729, 2013.

[25] N. Xie, J. Yang, and J. Shao, "Study on the hydromechanical behavior of single fracture under normal stresses," *KSCE Journal of Civil Engineering*, vol. 18, no. 6, pp. 1641–1649, 2014.

[26] L. C. Wang and M. B. Cardenas, "Development of an empirical model relating permeability and specific stiffness for rough fractures from numerical deformation experiments," *Journal of Geophysical Research - Solid Earth*, vol. 121, no. 7, pp. 4977–4989, 2016.

[27] I. W. Yeo, M. H. de Freitas, and R. W. Zimmerman, "Effect of shear displacement on the aperture and permeability of a rock fracture," *International Journal of Rock Mechanics and Mining Sciences*, vol. 35, no. 8, pp. 1051–1070, 1998.

[28] W. Yeo, "Effect of contact obstacles on fluid flow in rock fractures," *Geosciences Journal*, vol. 5, no. 2, pp. 139–143, 2001.

[29] C. Cao, Z. G. Xu, J. R. Chai, and Y. Q. Li, "Radial fluid flow regime in a single fracture under high hydraulic pressure during shear process," *Journal of Hydrology*, vol. 579, p. 124142, 2019.

[30] R. C. Liu, N. Huang, Y. J. Jiang, G. H. Han, and H. W. Jing, "Effect of shear direction change on shear-flow-transport processes in single rough-walled rock fractures," *Transport in Porous Media*, vol. 133, no. 3, pp. 373–395, 2020.

[31] J. B. Walsh, "Effect of pore pressure and confining pressure on fracture permeability," *International Journal of Rock Mechanics & Mining ences & Geomechanics Abstracts*, vol. 18, no. 5, pp. 429–435, 1981.

[32] Y. Chen, W. Liang, and J. Yang, "Study on the effective stress characteristic of rough rock fractures with water pressure," *Yanshilixue Yu Gongcheng Xuebao/Chinese Journal of Rock Mechanics and Engineering*, vol. 37, pp. 3850–3860, 2018.

[33] Y. D. Chen, H. J. Lian, W. G. Liang, J. F. Yang, V. P. Nguyen, and P. A. Stéphane, "The influence of fracture geometry variation on non-Darcy flow in fractures under confining stresses," *International Journal of Rock Mechanics and Mining Sciences*, vol. 113, pp. 59–71, 2019.

[34] L. M. Yin, W. J. Guo, and J. T. Chen, "Development of ture triaxial rock test system of coupled stress-seepage and its application," *Chinese Journal of Rock Mechanics and Engineering*, vol. 33, no. Supp.1, pp. 2820–2826, 2014.

[35] W. B. Sun, Y. Xue, L. Yin, and J. Zhang, "Experimental study on seepage characteristics of large size rock specimens under three-dimensional stress," *Geomechanics and Engineering*, vol. 18, no. 6, p. 567, 2019.

[36] Z. Chang, Y. Zhao, and Y. Hu, "Theoretical and experimental study on seepage law of single fracture under 3D stress," *Chinese Journal of Rock Mechanics and Engineering*, vol. 23, no. 4, pp. 620–624, 2004.

[37] Y. Kong, Z. D. Zhu, and H. N. Ruan, "Stress-seepage coupling characteristics of jointed rock mass under three principal stresses," *Rock and Soil Mechanics*, vol. 39, no. 6, pp. 1000–7598, 2018.

[38] Z. Z. Shen, F. Chen, and J. Zhao, "Experimental study on seepage characteristics of the intersection of tubular karst passage and fissure," *Journal of Hydraulic Engineering*, vol. 53, no. 2, pp. 137–145, 2008.

[39] H. Zhu and L. Han, "Experimental study on grouting seepage characteristics of single-fracture specimen under three-dimensional stress," *Arabian Journal of Geosciences*, vol. 15, no. 9, pp. 212–242, 2022.

[40] H. Zhu, L. Han, L. Meng, W. Dong, and S. Yan, "True triaxial experimental study on fluid flow in single fracture with different dip angles under three-dimensional stress at different depths," *Journal of Petroleum Science and Engineering*, vol. 211, p. 110193, 2022.

[41] Y. Wang, Z. Y. Song, T. Q. Mao, and C. Zhu, "Macro-meso fracture and instability behaviors of hollow-cylinder granite containing fissures subjected to freeze–thaw–fatigue loads," *Rock Mechanics and Rock Engineering*, vol. 55, no. 7, pp. 4051–4071, 2022.

[42] Y. Wang, Y. Su, Y. Xia, H. Wang, and X. Yi, "On the effect of confining pressure on fatigue failure of block-in-matrix soils exposed to multistage cyclic triaxial loads," *Fatigue and Fracture of Engineering Materials and Structures*, vol. 45, no. 9, pp. 2481–2498, 2022.

[43] Y. Wang, J. Q. Han, Y. J. Xia, and D. Y. Long, "New insights into the fracture evolution and instability warning predication for fissure-contained hollow-cylinder granite with different hole diameter under multi-stage cyclic loads," *Theoretical and Applied Fracture Mechanics*, vol. 119, p. 103363, 2022.

[44] Y. Wang, T. Mao, Y. Xia, X. Li, and X. Yi, "Macro-meso fatigue failure of bimrocks with various block content subjected to multistage fatigue triaxial loads," *International Journal of Fatigue*, vol. 107014, 2022.